This is an electronic reprint of the original article.
This reprint *may differ* from the original in pagination and typographic detail.

Author(s): Rognoni, Lorenz; Stigler, Johannes; Pelz, Benjamin; Ylänne, Jari; Rief, Matthias

Title: Dynamic force sensing of filamin revealed in single-molecule experiments

Year: 2012

Version:

Please cite the original version:

Classification: BIOLOGICAL SCIENCES - Biophysics and Computational Biology

Dynamic force sensing of filamin revealed in single molecule experiments

Lorenz Rognoni[1], Johannes Stigler[1], Benjamin Pelz[1], Jari Ylänne[2], Matthias Rief[1,3,*]

[1]Physik Department E22, Technische Universität München, James-Franck-Straße, 85748 Garching, Germany

[2]Department of Biological and Environmental Science and Nanoscience Center, University of Jyväskylä, Jyväskylä, Finland

[3]Munich Center for Integrated Protein Science, 81377 München, Germany

[*]To whom correspondence should be addressed. E-mail: mrief@ph.tum.de

1

Mechanical forces are important signals for cell response and development, but detailed molecular mechanisms of force sensing are largely unexplored. The cytoskeletal protein filamin is a key connecting element between the cytoskeleton and trans-membrane complexes such as integrins or the von-Willebrand receptor GPIb. Here we show using single molecule mechanical measurements that the recently reported immunoglobulin domain pair 20-21 of human filamin A acts as an auto-inhibited force-activatable mechano-sensor. We developed a mechanical single molecule competition assay that allows online observation of binding events of target peptides in solution to the strained domain pair. We find that filamin force sensing is a highly dynamic process occurring in rapid equilibrium that increases the affinity to the target peptides by up to a factor of 17 between 2 and 5 pN. The equilibrium mechanism we find here can offer a general scheme for cellular force sensing.

Sensing of signals is key for every cell to adapt and react to changing environmental conditions. Such signals can be chemical, optical or even electrical in the case of nerve cells. In recent years, mechanical forces have been identified as important signals for cell development and cytokinesis. Mechanical signals have crucial implications for processes such as stem cell differentiation (1) or the remodeling of cardiac muscle tissue (2). Even though the sensing of mechanical forces has been postulated in various contexts, molecular mechanisms of force sensing have remained to a large degree elusive.

The cytoskeletal protein filamin is a dimeric actin cross-linker that acts as a signaling hub for various proteins (3). Two prominent examples for interaction partners are integrins (4-6) or glyco protein 1 b (GPIb), a constituent of a trans-membrane complex found in platelets that binds to von-Willebrand-factor during blood clotting (7-9). Both the filamin-integrin and the filamin-GPIb interactions have been shown to be exposed to mechanical forces in living cells (10, 11). The filamin monomer consists of an N-terminal actin-binding domain and a sequence of 24 immunoglobulin (Ig) domain repeats that form the filamin rod (Fig. 1A). Within the rod 2 region (Ig domains 16-23, see Fig. 1A), filamin can interact with trans-membrane protein complexes, thus establishing a mechanical connection between the cytoskeleton and the extracellular side. The major interaction sites within rod 2 are the odd numbered domains, specifically domains 17, 19 and 21. The trans-membrane interaction partners bind to these domains through a terminal peptide sequence that forms an additional β-strand extending the β-sheet structure of the domain (12, 13) (Fig. 1B).

In contrast to the linear arrangement of domains found in many structural proteins like titin, fibronectin or rod 1 of filamin, the Ig domains 18-21 of filamin's rod 2 are arranged in pairs (14, 15). In those pairs, the A-strand of the even numbered domains is not integrated into the domain structure but binds to the subsequent odd-numbered domain thus inhibiting the

interaction of this domain with its peptide ligand (Fig. 1A and Fig. S1). It has been proposed that this special arrangement into domain pairs effects a force sensing mechanism in filamin (Fig. 1B) (14, 16). Recent *in vitro* studies of mechanically strained filamin-crosslinked actin networks have provided further support for a potential force-sensing role of filamin (17).

In the present study, we have designed and performed single molecule mechanical measurements that provide direct evidence for a force-sensing mechanism of human filamin A. We show quantitatively at the single molecule level, how force increases the binding of interaction partners by shifting the conformational equilibrium of the auto-inhibited filamin domain pair 20-21 (FLNa20-21).

Results

Filamin domain 21 interaction with different tethered target peptides.

In a first set of experiments, we investigated the uninhibited mechanical binding strength of domain 21 to different interaction partners: the C-terminal peptide of GPIb's α-chain (GPIbα), the integrin β7 cytoplasmic tail peptide (ITβ7) as well as the filamin-interacting peptide of the integrin regulator migfilin (Mig) (18, 19). To this end, we fused the respective interacting peptides directly to the N-terminus of an isolated domain 21 of filamin (FLNa21) with a 6 amino acid residues spacer allowing the necessary flexibility (see SI). Force application to the molecular constructs was achieved by tethering the protein termini to 180 nm-long double-stranded DNA molecules through disulfide bonds. The ends of the DNA were functionalized with biotin and digoxigenin, respectively. This allowed attachment to 1 μm diameter silica beads that were manipulated in a dual beam optical trap (Fig. 1B, for details see SI) (20-22).

4

Upon stretching the DNA-protein construct, the force rises steeply beyond extensions of 320

nm, when the DNA is almost fully elongated (Fig. 2A). At forces between 7 and 12 pN, rapid

near-equilibrium fluctuations of binding and unbinding of the GPIbα peptide can be observed.

The contour length gain during this transition ($\Delta L = 12.5 \pm 0.5$ nm) is in excellent agreement

with the expected length gain if the 26 amino acid residues of the bound peptide detach and

are fully stretched (see Table S1 in the Supporting Information, SI). To obtain a precise

analysis of the force-dependent binding/unbinding kinetics of the peptide, we performed

measurements where the trap centers were held at a constant separation hence imposing a

constant average force-bias on the fluctuating molecule. Since only the separation of the

trapping potentials is held constant, the force varies between the closed and open

conformation. We define force-bias as the mean of the force acting on the closed/bound and

open/unbound state. This allowed us to observe fluctuations between bound (high force) and

unbound (low force) states for several minutes at different biasing forces (Fig. 2B). At low

forces, the molecule dwells predominantly in the bound state with few rapid excursions into

the unbound state (Fig. 2B, lower trace). With increasing force, the equilibrium (black

population distributions in Fig. 2B) shifts to the unbound state together with altered kinetics

(upper two traces of Fig. 2B). The force-dependent population shift provides a direct measure

for the free energy of binding in the absence of load of 10.6 $k_B T$ (see Fig. S2 and SI text). A

dwell-time analysis using a Hidden-Markov-Model (HMM) (22, 23) yields the force-

dependent kinetics of GPIbα binding/unbinding (Fig. 2C). Unbinding rates (circles) increase

with force, while binding rates (triangles) drop with force. For extrapolation of the

binding/unbinding branches to zero-force, we used a model that considers the compliance of

the unfolded peptide leading to a curvature in the branches (21). The slopes of the

binding/unbinding branches reflect the distance of the transition state from the unbound and

bound state, respectively. The sum of those distances (12.3 nm, measured in contour length)

as obtained from the fits, is very close to the total contour length of the peptide (12.5 nm), which supports the validity of the analysis. The fast binding rate at zero-load of 34,000 s^{-1} reflects the effectively high concentration of the ligand due to tethering. For the unbinding rate, we find 1.9 s^{-1} (see Table S2).

In comparison to GPIbα, the ITβ7 ligand exhibits a significantly lower unbinding force (Fig. 2D) as well as free energy of binding (5.8 $k_B T$, see Fig. S2). The major difference in kinetics (Fig. 2 E and F) results from a much faster unbinding rate of 120 s^{-1} at zero-load while the binding rates are similar to the ones of GPIbα (see Table S2). Since the unbinding lengths of the tethered ligands and hence the effective concentrations for both peptides are identical, the similar binding rates indicate that rebinding speed is not influenced by details of the sequence. This is further supported by our data of migfilin (Fig. 2 G-I) that exhibits very similar binding rates. The unbinding rates and the binding free energy of migfilin (6.5 $k_B T$) are in between those of GPIbα and ITβ7 (Fig. S2). GPIbα exhibits by far the strongest binding to filamin of all peptides investigated. This finding is particularly important, since platelet integrity critically depends on the mechanical strength of this bond once attached to von-Willebrand-factor during blood clotting (11). It has been shown that GPIbα binds von-Willebrand-factor on the extracellular side with forces similar to those we find for intracellular filamin-binding (24). This could provide a stable mechanism to transmit force from the extracellular space to the actin cytoskeleton. The higher free energies of binding and interaction forces of migfilin relative to ITβ7 are consistent with migfilin's role in competing off the cytoplasmic tail of β-integrins from filamin during talin-mediated integrin activation (18, 19).

Single molecule mechanical competition assay: FLNa21 interaction with ligands in solution.

In their physiological context, the membrane protein tails are not tethered to the filamin domains. Even though our assay gives valuable information about the unbinding kinetics under load, measuring the free binding and unbinding rates of the ligands requires a different experimental approach. Fluorescent single molecule methods cannot be used at the high concentrations necessary for observing binding (up to 100 µM) due to the associated high background. We therefore developed a mechanical single molecule assay that allows direct observation of binding/unbinding events of freely diffusing ligands at those concentrations. To this end, we observed the opening and closing fluctuations of a tethered GPIbα-FLNa21 construct in the presence of freely diffusing GPIbα peptide in solution (Fig. 3A). Under load, the tethered ligand will constantly fluctuate between bound and unbound states as shown above (Fig. 3A, left cartoon). If the construct is in an open conformation, there will be a competition between the tethered ligand rebinding and a free ligand binding from solution. In the latter case (Fig. 3A, right cartoon), rebinding of the tethered ligand will be suppressed and the opening/closing fluctuations should vanish until the bound ligand spontaneously dissociates. A sample trace is shown in Fig. 3A where fluctuating states (high standard deviation (σ)) can be clearly distinguished from mechanically quenched states (low σ). A zoom into this trace (Fig. 3B) shows that in the fluctuating state (left), the construct undergoes rapid opening and closing transitions, while in the quenched state (right), the construct dwells in the open conformation (see Fig. S3 for sample traces at different forces). The dwell times in the fluctuating state ($\tau_{unbound}$) as well as in the quenched state (τ_{bound}) now provide direct information about the binding kinetics of the ligand from solution. While $1/\tau_{bound}$ directly yields the off-rate, $1/\tau_{unbound}$ depends on both the solution concentration of the ligand and the applied force:

7

$$\frac{1}{\tau_{\text{unbound}}} = k_{\text{on}} \cdot [\text{GPIb}\alpha] \cdot P_{\text{open}}(F),$$

where k_{on} is the pseudo first-order on-rate, $[\text{GPIb}\alpha]$ is the concentration of ligand and $P_{\text{open}}(F)$ is the force dependent probability for the tethered ligand to be in the open conformation (Fig. S2). We measured τ_{bound} and τ_{unbound} as a function of force and at two different ligand concentrations (Fig. 3C). As expected, τ_{unbound} decreases with force, since the probability for finding the tethered construct in an open conformation increases. Moreover, τ_{unbound} decreases with increasing solution concentration. From the fits to the concentration-dependent τ_{unbound}-curves we obtain a pseudo first-order on-rate for GPIbα binding of $k_{\text{on}} = 3.7$ (μM*s)$^{-1}$. It is important to note that the shape of the fit curves is pre-determined by $P_{\text{open}}(F)$, which is not a fit parameter but measured directly (Fig. S2). The off-rate ($1/\tau_{\text{bound}}$) is independent of concentration as well as applied force and we find $k_{\text{off}} = 1.8$ s^{-1}. We note that this value is very close to the zero-force value that we extrapolated from the tethered construct in Fig. 2C. This again confirms the validity of the extrapolation methods used above.

The new competition assay now allows to determine the force-free on- and off-rates for all three different peptides (Table S3 and Fig. S4 A and B). Even though the binding kinetics of those ligands have not been measured before, the equilibrium binding constants (K_D) of the three peptides calculated from the kinetics agree well with bulk measurements (Table S3) (25). It is interesting to note that with K_D's in the micromolar range and above, as well as lifetimes below a second, all those interactions are very dynamic.

Mechanical response of the auto-inhibition of FLNa20-21.

In a next set of experiments, we utilized the single molecule mechanical competition assay to investigate the force-sensing mechanism of the domain pair FLNa20-21 (16). Can we see an auto-inhibited conformation of the FLNa20-21 domain pair that is relieved with increasing loads? A force vs. extension curve of this domain pair is shown in Fig. 4A. Upon stretching (blue trace), we observe two major unfolding peaks around 15 and 37 pN, respectively. The lower peak exhibits a contour length change of $\Delta L = 17.7 \pm 0.3$ nm and the higher peak has a ΔL of 28.8 ± 0.5 nm. The lower force peak can be directly associated with unfolding of domain 20, while the high peak reflects unfolding of domain 21. This assignment is confirmed by measurements with the isolated domains 20 and 21 (Fig. S5). Compared to other Ig domains of filamin (26-28), domain 20 appears much more mechanically labile.

A clear signal for opening the auto-inhibited conformation, in which the A-strand of domain 20 is attached to domain 21, cannot be observed in the low resolution trace of Fig. 4A. The single molecule mechanical competition assay described above (Fig. 3) now offers a possibility to study the force dependent relief of auto-inhibition and hence the force-sensing properties of the domain pair together with its force-dependent binding rate of ligands from solution. At a solution concentration of 2.7 μM GPIbα, a force-dependent change in the fluctuation pattern of the domain pair can be observed when held at a biasing force of 4.5 pN (Fig. 4B). Again, rapidly fluctuating high-σ regions are interrupted by quenched low-σ dwells. The quenched levels (e.g. right arrow in Fig. 4B) exhibit exactly the same lifetimes of GPIbα unbinding ($\tau_{bound} = 520$ ms) as in Fig. 3C. The high-σ regions in the high-bandwidth trace (left arrow) also reflect the same concentration-dependence and pseudo first-order on-rate as before (Fig. S4C), which confirms the unbinding and rebinding of GPIbα peptides from solution. A zoom into the high-σ region (Fig. 4B, inset) reveals that the molecular construct

9

undergoes rapid transitions between a closed and an open form. Force directly affects the probability of GPIbα binding to the domain pair from solution. This can be seen in the strongly smoothed curves of Fig. 4C where increasing load increases the number of binding events observed. It is important to note that the force conditions shown were measured using the same molecule. The length change we observe between the closed and open conformation is 1.4 nm at a biasing force of 3.2 pN. From this length change, we can calculate a total contour length difference between the closed and open conformation of 14.5 ± 1.1 nm. This value is very close to the calculated contour length gain of 16.8 nm of a conformational change where the A-strand of FLNa20 detaches from FLNa21 and the domain pair opens up, as suggested by the crystal structure (14). Combining the force and concentration-dependent binding kinetics of GPIbα to FLNa20-21 allows reconstruction of the force-dependent gating-characteristics of the domain pair. In Fig. 4D, three data sets at different peptide concentrations were normalized by their maximal peptide binding rates, giving a direct measurement of the force-dependent opening probabilities (for details see SI). The solid line represents the globally fitted opening probability with a force of half maximal opening $F_{1/2} =$ 3.9 pN and a total free energy for opening of 2.8 k_BT. Independently, the force-dependent opening probability of FLNa20-21 was obtained (Fig. 4D, dashed line) from dwell time analysis of the unquenched regions using HMM analysis (see Fig. S6 and SI text).

Discussion

The force-gating characteristic we find for FLNa20-21 is tuned to surprisingly low forces. For comparison, the putative force-sensing titin-kinase domain acting in the high-force environment of muscle was reported to undergo force-activation at around 40 pN (15, 29). However, *in vivo* and *in vitro* studies of the adhesion forces of integrins to fibronectin as well as the direct force-measurements within load-bearing focal adhesion of living cells have

10

indicated that a relevant force scale within cells may be much lower: on the order of a few pN (30-32). The force sensing of filamin seems to be tuned exactly to this force range. Another important aspect of the force sensing of filamin is its smooth opening characteristic. Unlike the common description of force induced structural changes within proteins as all or none events far from equilibrium, we find that filamin shifts its opening probability in a force-dependent and gradual manner from closed to open as indicated in the curve of Fig. 4D. This ensures a precise and well-controlled gating curve even though the involved binding energies lie below 4 $k_B T$. It has been argued that an auto-inhibition of filamin seems unlikely in *in vitro* experiments, since it could be shown that an excess of ligand alone is able to convert the filamin domain pairs from a closed to an open conformation (33, 34). However, this stood in apparent contrast to earlier reports that the isolated domain 21 binds stronger to ligands than the domain pairs (14) as well as to binding studies on strained filamin-crosslinked actin networks (17). Our results are now able to reconcile this contradiction. Opening of the domain pair under load is, unlike a mechanical switch, a gradual process that shifts the binding constants by up to a factor of 17, and thus modulates affinity in a force-dependent manner.

A further important aspect of the force transmission through filamin is the transient and dynamic nature of the bonds involved. We find that even the strongest interaction of GPIbα with rod 2 domains of filamin, which critically determines platelet integrity under shear flow forces (11), is transient with a lifetime of less than a second even in the absence of force.

How can a cell sustain mechanical loads applied over much longer time-scales? A view of the complete force transmission network helps to resolve this issue. Filamin does not offer only a single binding site to trans-membrane receptors but instead, rod 2 has three reported domain pairs (Fig. 5). Therefore, in a dimer of filamin, many interaction sites act in concert leading to

11

a strong avidity effect. Since bond energies are additive, the lifetimes will increase exponentially, which leads to long-lasting multiple bonds. Interestingly, the binding to domain 17 is likely not auto-inhibited (15). The constitutively active domain 17 may be important for transiently recruiting filamin to the membrane receptor. The subsequent build-up of mechanical tension can then relieve the auto-inhibition of the other domains promoting strong anchoring. The necessity of multiple parallel bonds for stable anchoring is in accord with the idea that the multiple binding sites of filamin can also induce clustering of trans-membrane receptors (10, 25). Alternatively, filamin interactions may be substituted or stabilized by other adaptor molecules. In the case of GPIbα, a candidate for such a molecule is 14-3-3ζ, which is required for firm adhesion and one of the 14-3-3ζ binding sites on GPIbα overlaps with that of filamin (35). An analogous function could be taken by talin in the case of integrin-based adhesion (14, 36).

In conclusion, we have shown that the rod 2 domains of filamin act as force sensing domains that react to the small cytoskeletal forces acting in cells. The dynamic equilibrium switching of this force sensor may provide a prototype for other force sensors found in living systems.

Materials and Methods

The domain pair 20-21 of human filamin A was genetically inserted between two ubiquitins with terminal cysteines that served as spacers. For the tethered peptide construct, domain 20 was replaced by the filamin-binding region of GPIbα/ITβ7/migfilin, linked to FLNa21 via an additional 6 amino acid glycine-serine spacer. To the terminal cysteines of the construct thiol-modified DNA handles of a length of 180 nm were attached. In order to create a dumbbell

geometry, the other biotin/digoxigenin functionalized end was attached to micron-sized

neutravidin/anti-digoxigenin silica beads (see Fig. 1B). The beads were trapped in the foci of

a custom-built dual beam optical tweezers setup and subjected to stretch-and-relax cycles or a

constant force-bias with fixed trap positions. All measurements were performed in PBS (10

mM phosphate buffer, 2.7 mM potassium chloride and 137 mM sodium chloride, pH 7.4). For

the single molecule mechanical competition assay, peptides with the same sequence as the

tethered ones were added into the solution.

Transitions between states were detected using a Hidden-Markov-Model analysis on the

unfiltered raw data of the difference signal of the two traps. Complete descriptions of the

methods used are given in SI Materials and Methods.

References

1.   Engler AJ, Sen S, Sweeney HL, Discher DE (2006) Matrix elasticity directs stem cell lineage specification. *Cell* 126:677–689.

2.   Hoshijima M (2006) Mechanical stress-strain sensors embedded in cardiac cytoskeleton: Z disk, titin, and associated structures. *Am J Physiol Heart Circ Physiol* 290:H1313–25.

3.   Nakamura F, Stossel TP, Hartwig JH (2011) The filamins: organizers of cell structure and function. *Cell Adh Migr* 5:160–169.

4.   Glogauer M et al. (1998) The role of actin-binding protein 280 in integrin-dependent mechanoprotection. *J Biol Chem* 273:1689–1698.

5.   Gehler S et al. (2009) Filamin A-beta1 integrin complex tunes epithelial cell response to matrix tension. *Mol Biol Cell* 20:3224–3238.

6.   Jiang P, Campbell ID (2008) Integrin binding immunoglobulin type filamin domains have variable stability. *Biochemistry* 47:11055–11061.

7.   Ruggeri ZM, Orje JN, Habermann R, Federici AB, Reininger AJ (2006) Activation-independent platelet adhesion and aggregation under elevated shear stress. *Blood* 108:1903–1910.

8.   Nesbitt WS et al. (2009) A shear gradient-dependent platelet aggregation mechanism drives thrombus formation. *Nat Med* 15:665–673.

9.   Huizinga EG et al. (2002) Structures of glycoprotein Ibalpha and its complex with von Willebrand factor A1 domain. *Science* 297:1176–1179.

10.   Lynch CD et al. (2011) Filamin depletion blocks endoplasmic spreading and destabilizes force-bearing adhesions. *Mol Biol Cell* 22:1263–1273.

11.   Cranmer SL et al. (2011) High shear-dependent loss of membrane integrity and defective platelet adhesion following disruption of the GPIbα-filamin interaction. *Blood* 117:2718–2727.

12.   Nakamura F et al. (2006) The structure of the GPIb-filamin A complex. *Blood* 107:1925–1932.

13.   Kiema T et al. (2006) The molecular basis of filamin binding to integrins and competition with talin. *Mol Cell* 21:337–347.

14.   Lad Y et al. (2007) Structure of three tandem filamin domains reveals auto-inhibition of ligand binding. *EMBO J* 26:3993–4004.

15.   Heikkinen OK et al. (2009) Atomic structures of two novel immunoglobulin-like domain pairs in the actin cross-linking protein filamin. *J Biol Chem* 284:25450–25458.

16.   Pentikainen U, Ylänne J (2009) The regulation mechanism for the auto-inhibition of binding of human filamin A to integrin. *J Mol Biol* 393:644–657.

17.   Ehrlicher AJ, Nakamura F, Hartwig JH, Weitz DA, Stossel TP (2011) Mechanical strain in actin networks regulates FilGAP and integrin binding to filamin A. *Nature* 478:260–263.

18.   Ithychanda SS et al. (2009) Migfilin, a molecular switch in regulation of integrin activation. *J Biol Chem* 284:4713–4722.

19.   Das M, Ithychanda SS, Qin J, Plow EF (2011) Migfilin and Filamin as Regulators of Integrin Activation in Endothelial Cells and Neutrophils. *PLoS ONE* 6:e26355.

20.   Cecconi C, Shank EA, Bustamante C, Marqusee S (2005) Direct observation of the three-state folding of a single protein molecule. *Science* 309:2057–2060.

21.   Gebhardt JCM, Bornschlögl T, Rief M (2010) Full distance-resolved folding energy landscape of one single protein molecule. *Proc Natl Acad Sci USA* 107:2013–2018.

22.   Stigler J, Ziegler F, Gieseke A, Gebhardt JCM, Rief M (2011) The complex folding network of single calmodulin molecules. *Science* 334:512–516.

23.   Stigler J, Rief M (2012) Hidden markov analysis of trajectories in single-molecule experiments and the effects of missed events. *Chemphyschem* 13:1079–1086.

24.   Kim J, Zhang C-Z, Zhang X, Springer TA (2010) A mechanically stabilized receptor-ligand flex-bond important in the vasculature. *Nature* 466:992–U123.

25.   Ithychanda SS et al. (2009) Identification and characterization of multiple similar ligand-binding repeats in filamin: implication on filamin-mediated receptor clustering and cross-talk. *J Biol Chem* 284:35113–35121.

26.   Furuike S (2001) Mechanical unfolding of single filamin A (ABP-280) molecules detected by atomic force microscopy. *FEBS Lett* 498:72–75.

27.   Schwaiger I, Kardinal A, Schleicher M, Noegel AA, Rief M (2004) A mechanical unfolding intermediate in an actin-crosslinking protein. *Nat Struct Mol Biol* 11:81–85.

28.   Chen H et al. (2011) Differential mechanical stability of filamin A rod segments. *Biophys J* 101:1231–1237.

29.   Puchner EM et al. (2008) Mechanoenzymatics of titin kinase. *Proc Natl Acad Sci USA* 105:13385–13390.

30.   Jiang G, Giannone G, Critchley DR, Fukumoto E, Sheetz MP (2003) Two-piconewton slip bond between fibronectin and the cytoskeleton depends on talin. *Nature* 424:334–337.

31.   del Rio A et al. (2009) Stretching single talin rod molecules activates vinculin binding. *Science* 323:638–641.

32. Grashoff C et al. (2010) Measuring mechanical tension across vinculin reveals regulation of focal adhesion dynamics. *Nature* 466:263–266.

33. Ithychanda SS, Qin J (2011) Evidence for multisite ligand binding and stretching of filamin by integrin and migfilin. *Biochemistry* 50:4229–4231.

34. Pentikainen U et al. (2011) Assembly of a filamin four-domain fragment and the influence of splicing variant-1 on the structure. *J Biol Chem* 286:26921–26930.

35. Yuan Y et al. (2009) Identification of a novel 14-3-3zeta binding site within the cytoplasmic domain of platelet glycoprotein Ibalpha that plays a key role in regulating the von Willebrand factor binding function of glycoprotein Ib-IX. *Circ Res* 105:1177–1185.

36. Roca-Cusachs P, Gauthier NC, del Rio A, Sheetz MP (2009) Clustering of alpha (5)beta (1) integrins determines adhesion strength whereas alpha (v)beta (3) and talin enable mechanotransduction. *Proc Natl Acad Sci USA* 106:16245–16250.
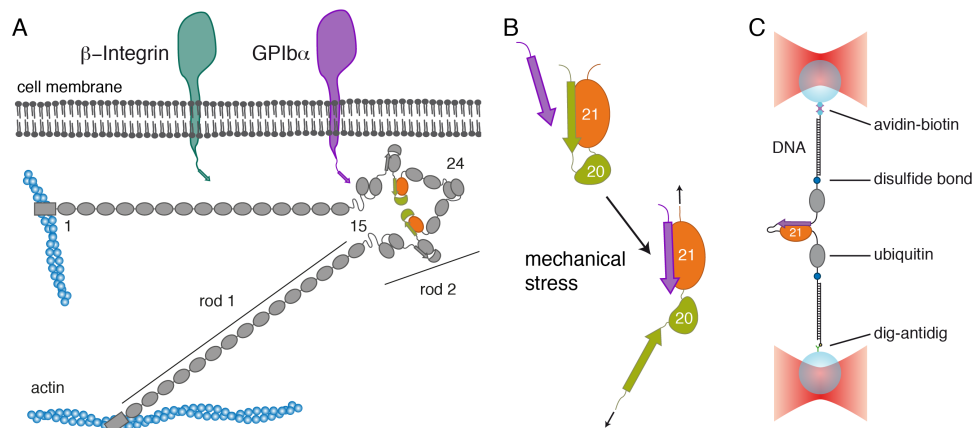
Figures

Fig. 1. Interaction of filamin with trans-membrane proteins. (A) Schematics of the domain arrangement of filamin and its interaction with the trans-membrane proteins integrin and GPIbα. Filamin consists of 24 immunoglobulin domains that dimerize at domain 24 and carry an N-terminal actin-binding domain. In its rod 2 region (Ig domains 16-24), domains 16-21 (FLNa16-21) arrange in pairs that contain binding sites for integrins (dark green) and GPIbα (purple). The domain pair FLNa20-21 is highlighted in orange and green. (B) Detailed arrangement of the domain pair FLNa20-21. The A-strand of FLNa20 binds to FLNa21 thus auto-inhibiting its interaction with the trans-membrane proteins (upper cartoon). It has been hypothesized that mechanical stress releases the auto-inhibition and promotes interaction with the targets (lower cartoon). (C) Schematics of the single molecule assay using a double beam optical trap (see text and SI).
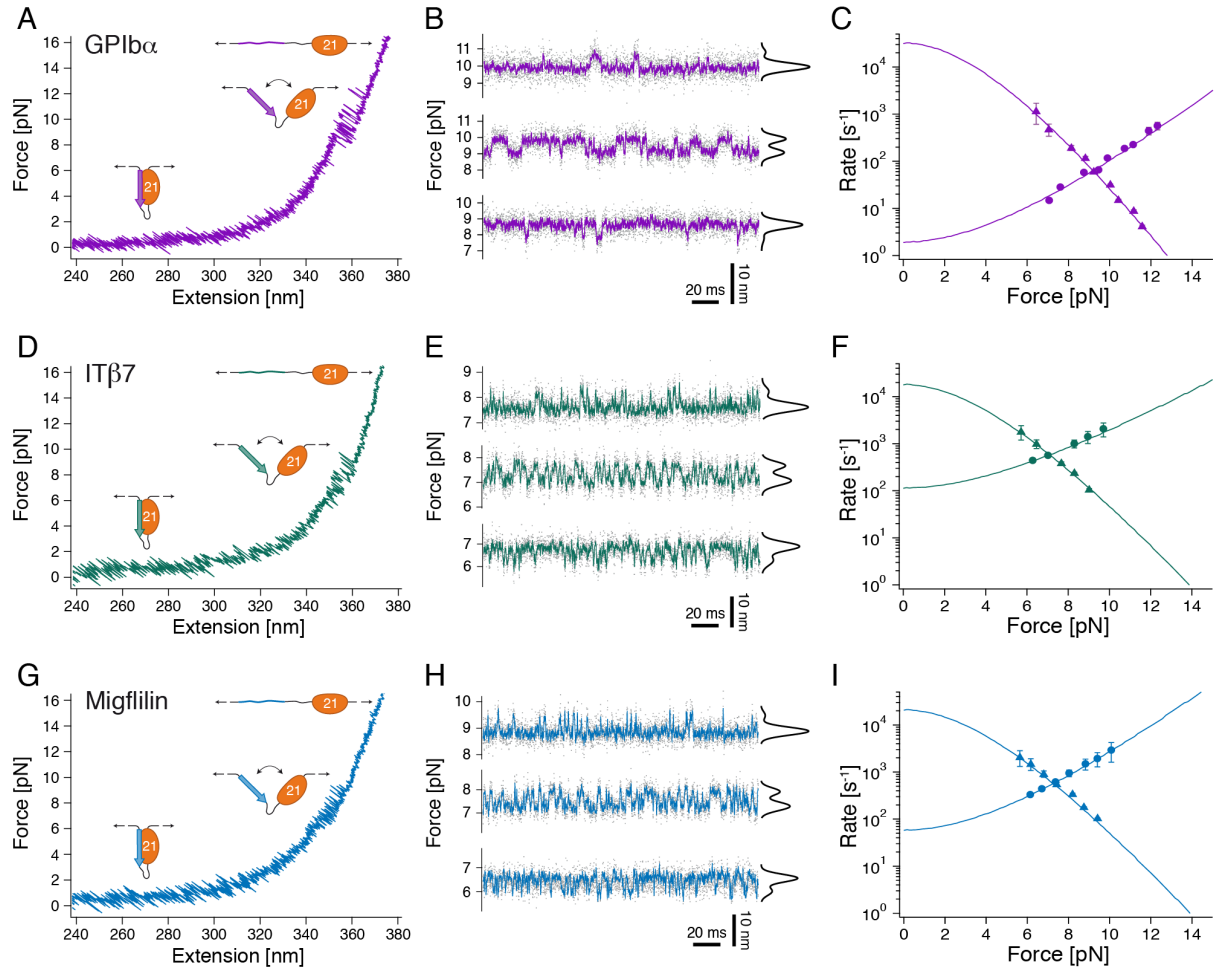
17

Fig. 2. Interaction of filamin with tethered peptides. (A) Force-extension trace of the interaction between the target peptide of GPIbα and FLNa21 (GPIbα-FLNa21). At forces around 10 pN, the target peptide rapidly fluctuates between bound and unbound conformations and stays permanently unbound at higher loads (> 12 pN). (B) Equilibrium traces obtained at three different biasing forces. At high loads (upper trace), the probability (black histogram) is shifted to the unbound state, while at decreasing loads, the bound state becomes more and more populated (lower 2 traces). (C) Opening (circles) and closing (triangles) rates as a function of force. The solid line is an extrapolation of the rates to zero-load taking into account the compliance of all mechanical elements in the construct (see SI). (D) Force-extension trace of the interaction between the target peptide of β7-integrin and FLNa21 (ITβ7-FLNa21). (E) Equilibrium traces of ITβ7-FLNa21 obtained at three different biasing forces (cf. (B)). (F) Opening (circles) and closing (triangles) rates as a function of force (cf. (C)). (G) Force-extension trace of the interaction between the target peptide of migfilin and FLNa21 (Mig-FLNa21). (H) Equilibrium traces of Mig-FLNa21 obtained at three different biasing forces (cf. (B, E)). (I) Opening (circles) and closing (triangles) rates as a function of force (cf. (C, F)).
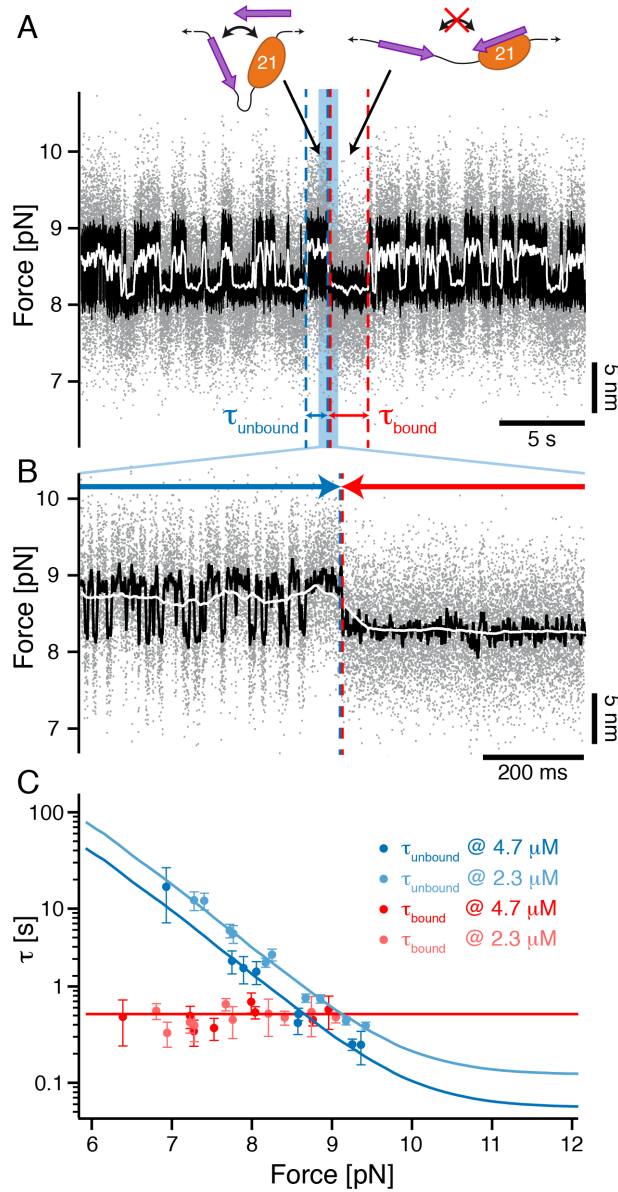
18

Fig. 3. Single molecule mechanical competition assay to study peptide binding from solution. (A) Time traces of opening and closing of the GPIbα-FLNa21 construct held at a force-bias of 8.5 pN in the presence of 2.3 μM GPIbα peptide in solution. The colored traces correspond to the 20 kHz data (grey), moving average filtered with 2.5 ms (black) and 50 ms (white) time window. Apparent high-σ (high standard deviation) regions with lifetimes $\tau_{unbound}$ in the black and grey traces are interrupted by low-σ regions with lifetimes τ_{bound}. (B) A zoom into the blue region shows the transition between a high-σ (rapid opening and closing cycles of the tethered construct) and low-σ region (blocked fluctuations due to competitive peptide binding from solution). (C) Dependence of the bound and unbound lifetimes as a function of applied force and solution concentration. As expected for binding from solution, $\tau_{unbound}$ depends on the opening probability of the tethered construct and hence the applied force, as well as the solution concentration while τ_{bound} is independent (see text and SI).
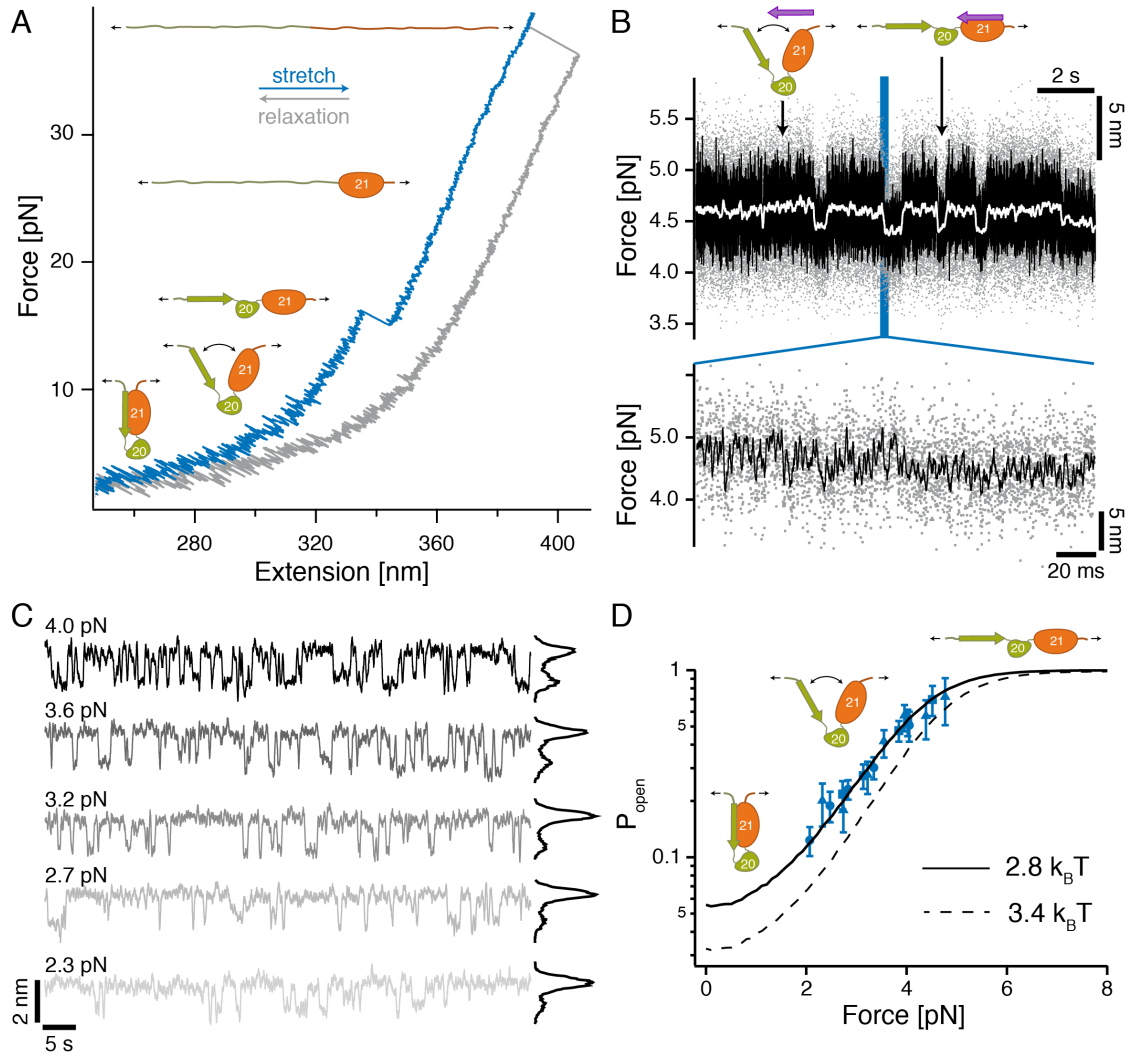
19

Fig. 4. Filamin domain pairs act as a precisely tuned mechano-sensor. (A) Low resolution stretch (blue) and relax (grey) trace of FLNa20-21. At forces around 15 pN, FLNa20 unfolds and at higher loads exceeding 30 pN, FLNa21 unfolds. Opening of the domain pair and release of the auto-inhibition is not visible at this experimental resolution. (B) Upper: competition assay of domain pair opening in the presence of 2.7 μM GPIbα peptide in solution observed at loads of 4.5 pN (color scheme as in Fig. 3A). High-σ regions (opening-closing fluctuations are interrupted with low-σ regions where bound peptide blocks fluctuations). Lower: zoom into a transition region. (C) Force-dependent binding of peptide from solution observed at biasing forces from 2.3 to 4.0 pN. From low to high loads, the binding probability (black histograms) increases constantly. (D) Force-dependent gating characteristics of the force-sensing domain pair as obtained from the force and concentration dependent dwell times of Fig. S4C (blue data points, black solid line shows global fit). The three symbols (triangle, square and circle) denote three different solution concentrations. The dashed black line is an independent measure of the force-dependent opening probability as obtained from the HMM analysis of the fluctuating state where no ligand from solution is bound (Fig. S6A).

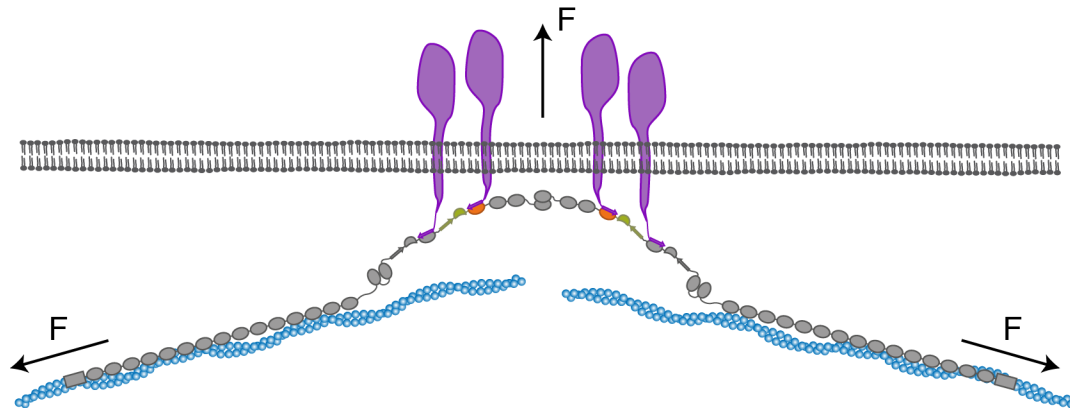**Fig. 5.** Model of the force-dependent binding and clustering of membrane receptors to filamin. Mechanical force in a strained cytoskeleton will lead to domain-pair opening in the rod 2 segment of filamin allowing the binding to membrane receptors. The simultaneous interaction with many domain pairs will significantly stabilize the cytoskeleton-membrane interaction and potentially induce clustering of receptors.

Supplementary Information for

Dynamic Force Sensing of Filamin Revealed in Single Molecule Experiments

Lorenz Rognoni, Johannes Stigler, Benjamin Pelz, Jari Ylänne, Matthias Rief

correspondence to: mrief@ph.tum.de

This PDF file includes:

Supporting Materials and Methods

Tables S1 to S3

Figs. S1 to S6

Supporting Materials and Methods

Molecular cloning
All protein constructs were inserted between two ubiquitin domains with terminal cysteines using molecular cloning techniques and expressed in *E. coli.* The ubiquitins serve as spacer-molecules to prevent direct reaction of the terminal cysteines later used for DNA-handle coupling. Since ubiquitin domains are mechanically much more stable than Ig domains (1), they do not unfold at our exerted force range and thus do not interfere during the single molecule mechanical measurements.

To study the binding site of domain 21 of human filamin A, the corresponding 13-15 amino acid long binding regions of GPIbα, Migfilin and ITβ7 were tethered to the N-terminus of domain 21 via a flexible 6 amino acid glycine-serine-linker. The resulting amino acid sequences are the following:

GPIbα-FLNa21:

MACKMQIFVKTLTGKTITLEVEPSDTIENVKAKIQDKEGIPPDQQRLIFAGKQLEDGR
TLSDYNIQKESTLHLVLRLRGGELGGSGGPTFRSSLFLWVRPGGSGGSGPLGEGGAH
KVRAGGPGLERAEAGVPAEFSIWTREAGAGGLAIAVEGPSKAEISFEDRKDGSCGVA
YVVQEPGDYEVSVKFNEEHIPDSPFVVPVASPSSGGSGGTMQIFVKTLTGKTITLEVEP
SDTIENVKAKIQDKEGIPPDQQRLIFAGKQLEDGRTLSDYNIQKESTLHLVLRLRGGK
CLEHHHHHH

Migfilin-FLNa21:

MACKMQIFVKTLTGKTITLEVEPSDTIENVKAKIQDKEGIPPDQQRLIFAGKQLEDGR
TLSDYNIQKESTLHLVLRLRGGELGGSGGPEKRVASSVFITLAPGGSGGSGPLGEGGA
HKVRAGGPGLERAEAGVPAEFSIWTREAGAGGLAIAVEGPSKAEISFEDRKDGSCGV
AYVVQEPGDYEVSVKFNEEHIPDSPFVVPVASPSSGGSGGTMQIFVKTLTGKTITLEV
EPSDTIENVKAKIQDKEGIPPDQQRLIFAGKQLEDGRTLSDYNIQKESTLHLVLRLRGG
KCLEHHHHHH

ITβ7-FLNa21:

MACKMQIFVKTLTGKTITLEVEPSDTIENVKAKIQDKEGIPPDQQRLIFAGKQLEDGR
TLSDYNIQKESTLHLVLRLRGGELGGSGGPLYKSAITTTINPGGSGGSGPLGEGGAHK
VRAGGPGLERAEAGVPAEFSIWTREAGAGGLAIAVEGPSKAEISFEDRKDGSCGVAY
VVQEPGDYEVSVKFNEEHIPDSPFVVPVASPSSGGSGGTMQIFVKTLTGKTITLEVEPS
DTIENVKAKIQDKEGIPPDQQRLIFAGKQLEDGRTLSDYNIQKESTLHLVLRLRGGKC
LEHHHHHH

Bold characters denote the peptide binding regions while the underlined sequence corresponds to domain 21 of human filamin A.

For investigation of the auto-inhibition mechanism, the following amino acid sequence of domains 20 and 21 was used. To prevent further undesired disulfide bonds in the two-domain

construct, one cysteine in domain 21 (Cys2293, all numbers are used as in the crystal structure, PDB ID code 2J3S) and two in domain 20 of human filamin A were mutated to serines (Cys2160, Cys2199).

FLNa20-21:

MACKMQIFVKTLTGKTITLEVEPSDTIENVKAKIQDKEGIPPDQQRLIFAGKQLEDGR
TLSDYNIQKESTLHLVLRLRGGELGGSGGSGEGRVKESITRRRRAPSVANVGSHSDLS
LKIPEISIQDMTAQVTSPSGKTHEAEIVEGENHTYSIRFVPAEMGTHTVSVKYKGQHV
PGSPFQFTV<u>GPLGEGGAHKVRAGGPGLERAEAGVPAEFSIWTREAGAGGLAIAVEGP
SKAEISFEDRKDGSSGVAYVVQEPGDYEVSVKFNEEHIPDSPFVVPVASP</u>SSGGSGGT
MQIFVKTLTGKTITLEVEPSDTIENVKAKIQDKEGIPPDQQRLIFAGKQLEDGRTLSDY
NIQKESTLHLVLRLRGGKCLEHHHHHH

Protein-DNA construct formation and DNA handle formation

For coupling of functionalized DNA handles, a protocol (2) derived from Cecconi *et al.* (3) was used. The terminal cysteines of the protein construct were activated by DTDP and mixed with TCEP-activated 3' thiol groups of 34 base pairs ssDNA oligos. DNA handles of 180 nm length were generated via PCR from a lambda-phage template. As forward primers, an equal mixture of biotin and digoxigenin modified oligos was used while reverse primers contained an abasic site leaving a ssDNA overhang complementary to the protein-bound oligos. Mixture of the protein-oligo construct with the functionalized DNA handles leads to the desired DNA-protein construct. The additional reaction step including the oligos increases the DNA-protein-coupling efficiency.

Optical tweezers setup

For the single molecule mechanical measurements, an in-house custom build dual beam optical tweezers setup with back focal plane detection and one AOD-steerable beam was used as described by Gebhardt *et al.* (4). Trapped beads were calibrated with the technique introduced by Tolić-Nørrelykke *et al.* (5). Trap stiffness could be determined with an error of approximately 10% and varied between different experiments from 0.25 to 0.30 pN/nm. Data were acquired at a sampling rate of 100 kHz and averaged to 20 kHz before storage. Detailed data analysis was carried out after the experiment using the difference of both 20 kHz bead signals to increase the signal to noise ratio (6). The signals were corrected for both crosstalk due to depolarization and proximity of the beams.

Experimental procedure

Protein-DNA constructs were mixed with silica beads (1 μm diameter, Bangs Laboratories, Inc.), which were previously covalently functionalized with anti-digoxigenin Fab fragments (Roche). These constructs were subsequently mixed with streptavidin coated silica beads (1 μm diameter, Bangs Laboratories, Inc.). Measurements were carried out at room temperature in PBS (10 mM phosphate buffer, 2.7 mM potassium chloride and 137 mM sodium chloride, pH 7.4, at 25 °C), with an added oxygen scavenger system (26 U/ml glucose oxidase, 17,000 U/ml catalase, 0.65% glucose). The protein-DNA coupled beads were introduced into a flow cell consisting of a coverslip attached to a glass slide via Nescofilm (Bando Chemical Industries Ltd.) and pretreated with bovine serum albumin (Sigma-Aldrich Co.). Trapped

beads were brought into close proximity to build a bead-DNA-protein dumbbell. Protein-DNA concentrations were adjusted to only sparsely cover the beads leading mainly to single tethered dumbbells. The trapping potentials were then separated with a constant velocity yielding force vs. extension traces or held at a constant separation to record force vs. time traces. When a dumbbell was successfully tested for single tether formation through stretch-and-relax cycles, further investigations of the reported equilibrium fluctuations followed at various constant trap positions. In the resulting force vs. time traces, the state population and dwell times were determined using Hidden-Markov-Model analysis.

Force vs. extension curves
During constant velocity experiments, where the position of the steerable trapping potential is moved with a constant speed, force vs. extension curves were recorded as shown in Fig. 2 A, D and G. The curve shape could be reproduced with a model describing the elasticity of a DNA-protein-chain. For the low force regime, where the protein is still folded and all tethered ligands bound, the elasticity of the DNA handles could be modeled with an extensible worm like chain model (eWLC). In this model the force is given by

$$F_{\mathrm{eWLC}}(d_{\mathrm{DNA}}) = \frac{k_{\mathrm{B}}T}{p_{\mathrm{DNA}}}\left(\frac{1}{4\left(1 - \frac{d_{\mathrm{DNA}}}{L_{\mathrm{DNA}}} - \frac{F}{K}\right)^2} - \frac{1}{4} + \frac{d_{\mathrm{DNA}}}{L_{\mathrm{DNA}}} - \frac{F}{K}\right) \qquad (1)$$

with persistence length p_{DNA}, contour length L_{DNA}, elastic modulus K and extension d_{DNA}. The fit yielded persistence lengths of approximately 20 nm, contour lengths of approximately 360 nm and elastic moduli of approximately 600 pN.

After unbinding of a tethered ligand or unfolding of the protein, a flexible polypeptide chain adds to the compliance of the DNA-protein construct. To account for this, the eWLC describing the DNA with the previously determined parameters was applied in series to a worm like chain model (WLC) (7) for the protein:

$$F_{\mathrm{WLC}}(d_{\mathrm{prot}}) = \frac{k_{\mathrm{B}}T}{p_{\mathrm{prot}}}\left(\frac{1}{4\left(1 - \frac{d_{\mathrm{prot}}}{L_{\mathrm{prot}}}\right)^2} - \frac{1}{4} + \frac{d_{\mathrm{prot}}}{L_{\mathrm{prot}}}\right) \qquad (2)$$

with persistence length p_{prot} set to 0.7 nm, contour length L_{prot} and extension d_{prot}.

For forces over 30 pN, the trapping potentials are no longer ideally linear, leading to a slight curvature in the force-extension traces. Therefore the WLC model was applied only for forces below 30 pN.

Contour length increases
Unfolding or tethered ligand unbinding leads to change in contour length of a stretched polypeptide chain. For all investigated constructs the contour length changes were determined

through the contour length difference of the fitted WLC models (Table S1). The corresponding theoretical values were calculated by subtracting the contour length contribution of the final conformational state from the initial contour length. Contributions of folded parts were measured from the crystal structure of the three domains 19 to 21 of human filamin A (PDB ID code 2J3S). The unstructured amino acid sequence contour length was calculated by multiplying the average contour length per amino acid of 3.65 Å by the number of residues.

Constant distance

To investigate the reported equilibrium transitions caused by the tethered ligand binding and unbinding, the trapping potentials were held at a constant separation and the bead position was recorded over time giving force vs. time traces as shown in Fig. 2 B, E and H. A change of the trap separation causes a different force-bias leading to a shift of the equilibrium of state population. For further analysis, the dwell times for each state were determined via a Hidden-Markov-Model (HMM) analysis.

Hidden-Markov-Model analysis

A Hidden-Markov-Model analysis was performed on the 20 kHz raw data of the difference signal to assign each data point to one of the system's two states as described by Stigler *et al.* (8). In brief, the raw data (grey dots in Fig. 2 B, E and H) were coarse grained into typically 200 bins and a histogram of the smoothed data (colored lines in Fig. 2 B, E and H) was calculated in order to identify the initial level positions (maxima of peaks in black histogram in Fig. 2 B, E and H). The emission values were initialized with Gaussian representation of the states. Each iteration consisted of one pass of the Forward-Backward-Algorithm followed by a re-estimation of the emission probabilities based on the maximum state-probability of each data point. During the iteration process, the emission probabilities were not constrained to Gaussian shapes any more. Iterations were repeated until only negligible numbers of data points (typically less than 0.1%) were reclassified in each step. Afterwards, the lifetime distribution was computed for all assigned states and compared to single exponentials, which can be used as a measure for the performance of the algorithm. The transition probability matrix was adjusted manually to yield optimal lifetime distributions.

Transition rates

After the state assignment by HMM analysis, the off-rates were obtained from single exponentials fitted to the lifetime distributions of each state. Since the tethered peptide binding is well-described by a two-state system, this directly gives the transition rates.

The single exponential fits were applied to normalized integrated lifetimes and took into account that events shorter than a dead time $\tau_{\min}$ or longer than $\tau_{\max}$ could not be observed:

$$p(t) = \frac{\exp(-k_{\mathrm{off}}\, t) - \exp(-k_{\mathrm{off}}\tau_{\min})}{\exp(-k_{\mathrm{off}}\, \tau_{\max}) - \exp(-k_{\mathrm{off}}\tau_{\min})} \tag{3}$$

with $\tau_{\max}$ set to the trajectory's length while $\tau_{\min}$ depended on the applied force bias and ranged between 200 and 800 μs. The extracted rates were afterwards corrected for missed

events. The whole analysis procedure is described by Stigler *et al.* in detail for the general case of a n-state system (8).

Force-dependent probabilities and determination of equilibrium free energies
For both states, probabilities were calculated directly as the sum of all lifetime histograms for a respective state divided by the trace length. The accuracy of this estimation is limited by the finite measurement time. Therefore, uncertainties were estimated by Monte-Carlo simulations by generation of a trace ensemble based on the measured transition rates and their statistical error. The standard deviation of probabilities obtained from the resulting trace ensemble was assigned as probability error.

In the following calculations, the system bead-DNA-protein-DNA-bead has been simplified to the equivalent system bead-DNA-protein with one effective trap stiffness. The effective bead displacement is then the sum of both bead displacements and the DNA contour length is doubled.

In our constant distance measurements, the trap distances are held constant. Every length change of the protein will be associated with a change in tension, which has to be accounted for in the following calculations. Based on the linker parameters determined by fitting equations 1 and 2 to the stretch-and-relax curves, the energy $G_i(F_i)$ stored by the bead-DNA-protein dumbbell at a force F_i is given by

$$G_i(F_i) = G_i^0 + G_{\text{Bead}}(F_i) + G_{\text{DNA}}(F_i) + G_{\text{Protein}}(F_i) \tag{4}$$

with G_i^0 the free energy of the protein in state i,

$$G_{\text{Bead}}(F_i) = \frac{1}{2} x_i(F_i) F_i \tag{5}$$

the Hookean bead displacement energy,

$$G_{\text{DNA}}(F_i) = \int_0^{d_{\text{DNA},i}} F_{\text{eWLC},i}(d_{\text{DNA}}) \mathrm{d}d_{\text{DNA}} \tag{6}$$

the entropic energy of stretching of dsDNA, and

$$G_{\text{Protein}}(F_i) = \int_0^{d_{\text{prot},i}} F_{\text{WLC},i}(d_{\text{prot}}) \mathrm{d}d_{\text{prot}} \tag{7}$$

the entropic energy of stretching of the unfolded protein.

When the system undergoes a transition from an initial state i to final state j, the force changes from F_i to F_j and the energy difference is then given by

6

$$\Delta G_{ij}(F_i, F_j) = G_j(F_j) - G_i(F_i)$$
$$= \Delta G_{ij}^0 + \Delta G_{\text{Bead}}(F_i, F_j) + \Delta G_{\text{DNA}}(F_i, F_j) + \Delta G_{\text{Protein}}(F_i, F_j) \tag{8}$$

Since the probabilities are related to energies according to

$$\frac{P_j(F_j)}{P_i(F_i)} = \exp\left(-\frac{\Delta G_{ij}(F_i, F_j)}{k_B T}\right) \tag{9}$$

we can obtain the energy differences of the protein between states i and j by performing a global fit to the probability data with

$$P_i(F) = \frac{1}{1 + \sum_{j \neq i} \exp\left(-\frac{\Delta G_{ij}^0 + \Delta G_{\text{DNA}}(F, F_j) + \Delta G_{\text{Protein}}(F, F_j)}{k_B T}\right)} \tag{10}$$

and weights equal to the inverse of the errors calculated as described before.

The experimental uncertainty of the equilibrium free energy difference ΔG_{ij}^0 is dominated by the calibration error of the trap stiffness of about 10%.

Zero-load extrapolation of binding rates
Due to the well defined linear zipping geometry of the tethered peptide constructs, the contour length increase is a well-suited reaction coordinate. The force dependence of measured binding and unbinding rates was fitted with a model introduced previously by Schlierf *et al.* (4, 9) accounting for the energy differences of the DNA linker and bead displacement between the initial open/closed state i and the transition state T:

$$k_{ij}(F) = k_i^0 \exp\left(-\frac{\Delta G_{iT}^{\#}(F_i, F_T)}{k_B T}\right) \tag{11}$$

with k_i^0 the binding/unbinding rate constant at zero-load used as a fit parameter. The additional activation energy under force,

$$\Delta G_{iT}^{\#} = \Delta G_{\text{Bead}}(F_i, F_T) + \Delta G_{\text{DNA}}(F_i, F_T) + \Delta G_{\text{Protein}}(F_i, F_T) \tag{12}$$

consists of the contributions discussed previously. F_T denotes the force acting on the construct at the transition state T between initial state i and final state j.

The protein length change ΔL_{iT} associated with a transition from i to T defines the transition state distance measured in contour length to which the system has to contract/extend before binding/unbinding over the barrier occurs.

With this model we can extrapolate the binding and unbinding rates of the tethered peptide to zero-load over a force range of 6 pN. A standard for the applicability of this model is the fact that equilibrium free energies derived from the zero-force rates by $k_{\mathrm{B}}T \cdot \ln (k^0_{\mathrm{bind}}/k^0_{\mathrm{unbind}})$ lie close to the measured ΔG^0 values obtained from equilibrium populations of states (Table S2). Another test for consistency is the fact that the contour length increases to the transition state, $\Delta L_{\mathrm{open,T}}$ and $\Delta L_{\mathrm{closed,T}}$, add up to the total contour length ΔL (Tables S1 and S2).

In case of the zero-load unbinding-rate k^0_{unbind}, we can directly compare it to the off-rate determined by our single molecule competition assay. Rates extracted from both methods are in excellent agreement (Tables S2 and S3).

Brownian Dynamics simulations
In order to test the state assignment based on the HMM analysis, we performed simulations of our equilibrium measurements and afterwards analyzed these with the same procedures used for the original measurements. Therefore, we simulated the thermal movement of both beads in their traps using Brownian Dynamics (2, 10). Mimicking the experimental setup, the two beads were connected with a linker consisting of DNA, modeled by an eWLC (Eq. 1), in series with a worm-like chain term (Eq. 2). The contour length of the protein depended on the state (open/closed, Table S1), which was determined for each time step using a Monte Carlo generator. The transition probabilities used for the Monte Carlo generator were calculated from the rates determined in the experiment (Table S2). During the simulation, the response of the two beads to the length change of the protein was calculated using Brownian Dynamics. The signal was treated as in the original experiments. Therefore, data points were taken with 100 kHz and subsequently sampled down to 20 kHz. After the simulation of a full trajectory, the difference signal of the two beads was calculated and analyzed using the HMM method. An example for such a simulated trace is shown in Fig. S6D.

Single molecule mechanical competition assay
Binding and unbinding of ligands added into solution can be monitored online with the following newly developed single molecule mechanical competition assay.

A ligand is tethered as a probe to the domain containing the targeted binding site as described above. During a constant distance measurement with the tethered peptide construct, the same or a different ligand competing for the identical binding site is added into solution in a concentration around the K_{D}. In contrast to similar methods based on a fluorescent signal, we were able to measure ligand concentrations of up to 100 µM since the non-bound ligand in solution gives no mechanical signal. The trap positions were adjusted to the range where the reported equilibrium fluctuations of the tethered ligand could be observed. When the construct is in the unbound state, ligands from solution can bind the unoccupied binding site blocking it for the tethered ligand. This leads to an interruption of the tethered ligand's binding/unbinding fluctuations and the construct gets trapped in the open conformation (Fig. S3). According to its characteristic off-rate, the ligand unbinds and fluctuations of the tethered ligand start again. By increasing the trap distance, the state population equilibrium of the tethered ligand is shifted to the unbound state and the binding site gets more exposed leading to an increased number of binding events of the ligand in solution.

Compared to ligand added into solution (1-100 µM), the tethered ligand's effective concentration (calculated from measured on-rates of tethered and non-tethered ligand: ca. 10 mM) is at least two orders of magnitude higher. This correlates with a similar discrepancy in

dwell times of the open state. The fluctuations of the tethered ligand are much faster than the unbinding/binding events of the solution ligands (see zoom in Fig. S3B). Therefore we are able to separate between the quenched state and the force-induced fluctuations. To extract the dwell times of the fluctuating and quenched state, an HMM analysis is applied to appropriately smoothed data, where the fluctuating state is averaged to its mean position while the binding/unbinding of solution ligands are still resolved (white trace in Fig. 3 A and B). The inverse of the dwell time of the unbound state τ_{bound} corresponds directly to the force and concentration independent off-rate (Fig. 3C). On the other hand, the dwell time of the fluctuating state $\tau_{unbound}$ equals the product of pseudo first-order binding rate k_{on}, the concentration [ligand] and the force dependent probability of the tethered ligand to be found in the open state $P_{open}(F)$.

$$\frac{1}{\tau_{unbound}} = k_{on} \cdot [\text{ligand}] \cdot P_{open}(F)$$

To extract k_{on}, $\kappa := k_{on} \cdot [\text{ligand}]$ is fitted to the measured $\tau_{unbound}$-data (Fig. 3C). It is important to note that $P_{open}(F)$ was already determined in previous measurements without ligand in solution (Fig. S2) and only κ is optimized during fitting. Combined with the known ligand concentration [ligand], this directly gives k_{on}. An overview of all determined rates is given in Table S2.

The accessible force range of the competition assay is limited due to the force-dependence of the tethered probe peptide. At the lower limit, the tethered peptide is bound most of the time, thus blocking the binding site, and only very few binding events are observed. With increasing force this number rises thus improving the statistical outcome. Simultaneously, the equilibrium of the tethered ligand is shifted to the open state. Increased dwell times in the open state can cause missed binding events of ligands from solution, which have fast off-rates in the range of the force-induced off-rates. This would lead to an apparent force dependent decrease of the off-rate. Therefore, a constant off-rate is an excellent proof that no binding events are missed.

For the analysis, the fluctuating state is treated as one level (see white traces in Figs. 3, 4 and S2) with a mean position determined by averaging over the fluctuations. When the population distribution of the tethered ligand is shifted by force, also the average extension of the construct is shifted from the shorter closed to the longer open position, while the signal of the quenched state remains at the position of the open state. Thus, the signal difference between quenched and fluctuating state decreases for increasing forces (Fig. S3B, white traces). As a consequence, data points were only taken starting from forces where a reasonable number of binding events could be observed. At the upper limit we chose forces that lead to a 50% opening probability of the tethered ligand to ensure an exact separation between quenched and fluctuating state.

Analysis of FLNa20-21 opening
For the two-domain construct FLNa20-21, the probability to be in the open state $P_{open}(F)$ was determined with two independent methods.

Firstly, the equilibrium fluctuations were directly analyzed using the HMM state assignment, as done for the tethered peptide constructs (Fig. S6 A-C). Since the analysis was carried out near the resolution limit at very low forces, we additionally tested the performance of the

9

HMM analysis by reanalyzing data that was simulated using Brownian Dynamics and a Monte Carlo Model based on the parameters extracted from the original data (Fig. S6 D-F). Both the original data and the simulation are in excellent agreement, which confirms the validity of our HMM analysis for low force conditions.

Secondly, the probability to be in the open state P_{open} (F) could also be determined independently using the single molecule mechanical competition assay, as shown in Fig. 4D. P_{open} (F) is given by Eq. 10 and since ΔG_{DNA} and $\Delta G_{\text{Protein}}$ are given by the already determined linker parameters, only the free energy difference of the opening ΔG^0_{open} is added as fit parameter. $P_{\text{open}}(F)$ was globally fitted to several independent measurements carried out at three different concentrations. Fig. 4D shows the dwell times after normalization by division with $k_{\text{on}} \cdot$ [ligand], giving $P_{\text{open}}(F)$. The black line corresponds to the globally fitted $P_{\text{open}}(F)$ with a free energy of 2.8 $k_{\text{B}}T$. This agrees excellently with the value determined through the kinetic HMM analysis (3.4 $k_{\text{B}}T$, dashed line in Fig. 4D).

For a successful dwell time analysis, the baseline of long time traces (typically 100 s) at low forces (2 to 4 pN) has to be constant, as shown in Fig. 4C. Therefore low frequency drift was corrected for, by subtracting a manually adjusted spline.

References

1. Schlierf M, Li H, Fernandez JM (2004) The unfolding kinetics of ubiquitin captured with single-molecule force-clamp techniques. *Proc Natl Acad Sci USA* 101:7299–7304.

2. Stigler J, Ziegler F, Gieseke A, Gebhardt JCM, Rief M (2011) The complex folding network of single calmodulin molecules. *Science* 334:512–516.

3. Cecconi C, Shank EA, Bustamante C, Marqusee S (2005) Direct observation of the three-state folding of a single protein molecule. *Science* 309:2057–2060.

4. Gebhardt JCM, Bornschlögl T, Rief M (2010) Full distance-resolved folding energy landscape of one single protein molecule. *Proc Natl Acad Sci USA* 107:2013–2018.

5. Tolić-Nørrelykke SF et al. (2006) Calibration of optical tweezers with positional detection in the back focal plane. *Rev Sci Instrum* 77:103101.

6. Moffitt JR, Chemla YR, Izhaky D, Bustamante C (2006) Differential detection of dual traps improves the spatial resolution of optical tweezers. *Proc Natl Acad Sci USA* 103:9006–9011.

7. Bustamante C, Marko JF, Siggia ED, Smith S (1994) Entropic elasticity of lambda-phage DNA. *Science* 265:1599–1600.

8. Stigler J, Rief M (2012) Hidden markov analysis of trajectories in single-molecule experiments and the effects of missed events. *Chemphyschem* 13:1079–1086.

9. Schlierf M, Berkemeier F, Rief M (2007) Direct observation of active protein folding using lock-in force spectroscopy. *Biophys J* 93:3989–3998.

10. Manosas M et al. (2007) Force unfolding kinetics of RNA using optical tweezers. II. Modeling experiments. *Biophys J* 92:3010–3021.

11. Lad Y et al. (2007) Structure of three tandem filamin domains reveals auto-inhibition of ligand binding. *EMBO J* 26:3993–4004.

Tables

Construct	ΔL (nm)	ΔL_{calc} (nm)	$\Delta L_{\text{closed,T}} + \Delta L_{\text{open,T}}$ (nm)
FLNa21-ITβ7	11.6 ± 0.3	11.1	9.7
FLNa21-Mig	12.0 ± 0.5	11.9	10.9
FLNa21-GPIbα	12.5 ± 0.5	11.1	12.3
FLNa20-21 opening	14.5 ± 1.1	16.8	13.7
FLNa20	17.7 ± 0.3	18.0	n.d.
FLNa21	28.8 ± 0.5	29.5	n.d.

Table S1. Contour length increases. ΔL in column 2 is the experimentally determined contour length increase using the WLC model, which was applied to force-extension traces, as well as to constant distance measurements. Errors are given as the standard error of the mean. ΔL_{calc} in column 3 are calculated contour length increases based on the crystal structure (see SI text). In column 4, the sum of transition state positions (Table S2, columns 3 and 5) are given as determined by kinetic HMM analysis for constructs where equilibrium measurements were taken. For FLNa20 and FLNa21, no equilibrium measurements were done and therefore the value is not determined.

Construct	$\log_{10}(k_{\text{bind}}^0)$ (s^{-1})	$\Delta L_{\text{open,T}}$ (nm)	$\log_{10}(k_{\text{unbind}}^0)$ (s^{-1})	$\Delta L_{\text{closed,T}}$ (nm)	ΔG^0 ($k_{\text{B}}T$)
FLNa21-ITβ7	4.29 ± 0.20	6.5 ± 0.7	2.08 ± 0.16	3.2 ± 0.8	5.8 ± 0.6
FLNa21-Mig	4.49 ± 0.33	6.6 ± 1.1	1.78 ± 0.15	4.4 ± 0.7	6.5 ± 0.7
FLNa21-GPIbα	4.53 ± 0.21	7.7 ± 0.6	0.29 ± 0.09	4.5 ± 0.4	10.6 ± 1.1
FLNa20-21 opening	3.69 ± 0.06	7.0 ± 0.6	2.24 ± 0.01	6.7 ± 0.3	3.4 ± 0.3

Table S2. Rate fit parameters of tethered peptide constructs and the double domain construct. All calculations are based on a model including the compliance of all mechanical elements (Eq. 11). Errors are given as standard error of the mean. $\Delta L_{\text{open,T}}$ and $\Delta L_{\text{closed,T}}$ are the distances from the initial closed/bound or open/unbound state to the transition state T measured in contour length (see SI text). In column 6, the equilibrium free energy is given as determined by Eq. 10.

Construct	Competing peptide	Concentration (μM)	k_{on} ($(μM*s)^{-1}$)	k_{off} (s^{-1})	K_D (μM)
FLNa21-ITβ7	ITβ7	50	3.03 ± 0.21	147 ± 31	48 ± 12
	ITβ7	100	3.06 ± 0.12	163 ± 4	53 ± 6
	Mig	38	3.89 ± 0.26	91.7 ± 14.1	24 ± 5
FLNa21-Mig	Mig	7.6	3.61 ± 0.13	75.2 ± 7.5	21 ± 3
	Mig	38	3.01 ± 0.08	76.0 ± 2.5	25 ± 3
FLNa21-GPIbα	GPIbα	2.3	3.57 ± 0.43	1.93 ± 0.07	0.54 ± 0.09
	GPIbα	4.7	3.83 ± 0.21	1.95 ± 0.15	0.51 ± 0.07

Table S3. Rates of peptide binding from solution measured with the single molecule mechanical competition assay (see SI Materials and Methods). The uncertainty of K_D in column 6 was calculated assuming a 10% maximal error for the concentration. All other errors are given as the standard error of the mean.
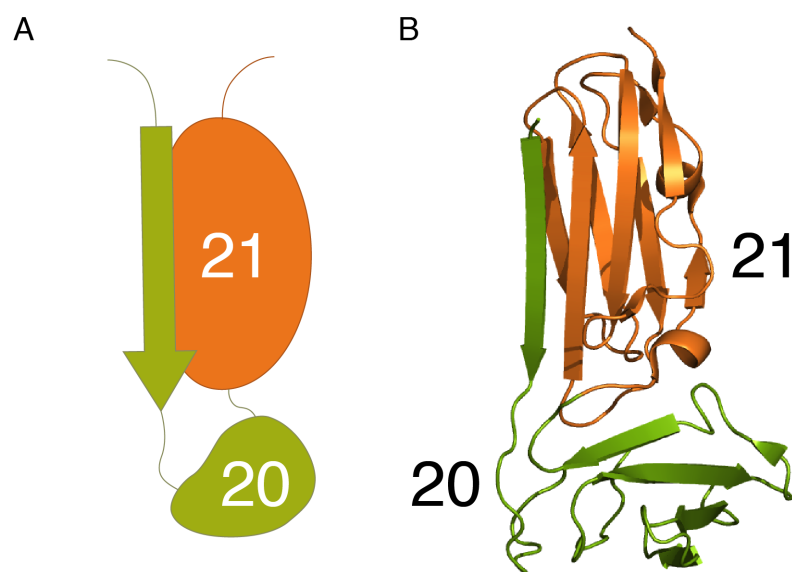
Figures

Fig. S1. Schematic representation of the structural arrangement of domains 20-21. The A-strand of domain 20 is not integrated into the domain structure but binds to the subsequent domain 21. (A) Simplified cartoon representation used in Fig. 1B. (B) Structural representation with same coloring as in (A) based on the crystal structure with PDB ID code 2J3S (11).
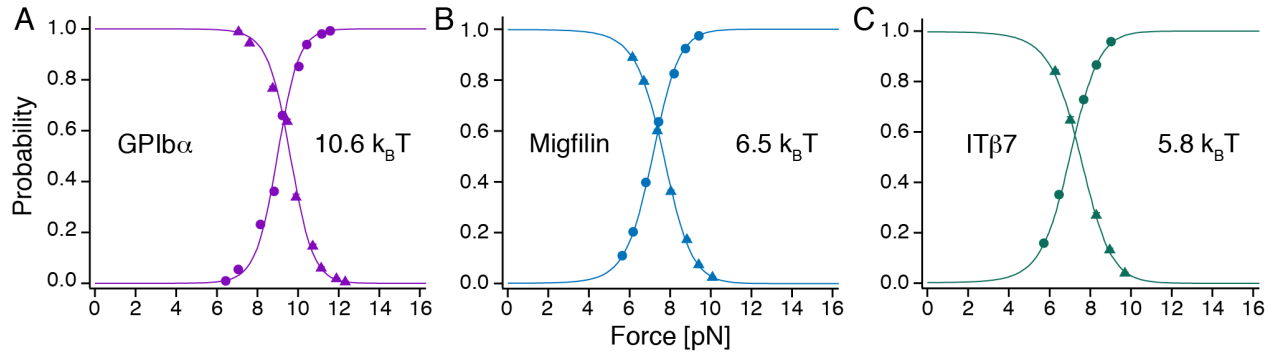
Fig. S2. Force dependent equilibrium probabilities of tethered peptide constructs to be in the bound (triangles) or unbound (circles) state. (A) GPIbα-FLNa21. (B) Mig-FLNa21. (C) ITβ7-FLNa21. Solid lines correspond to the globally fitted force dependent probability as given by Eq. 10. The only free fit parameter is the free binding energy of each peptide. The probabilities for the bound and unbound state do not add up to one since in our constant distance measurements the force is not constant for the bound and unbound state.
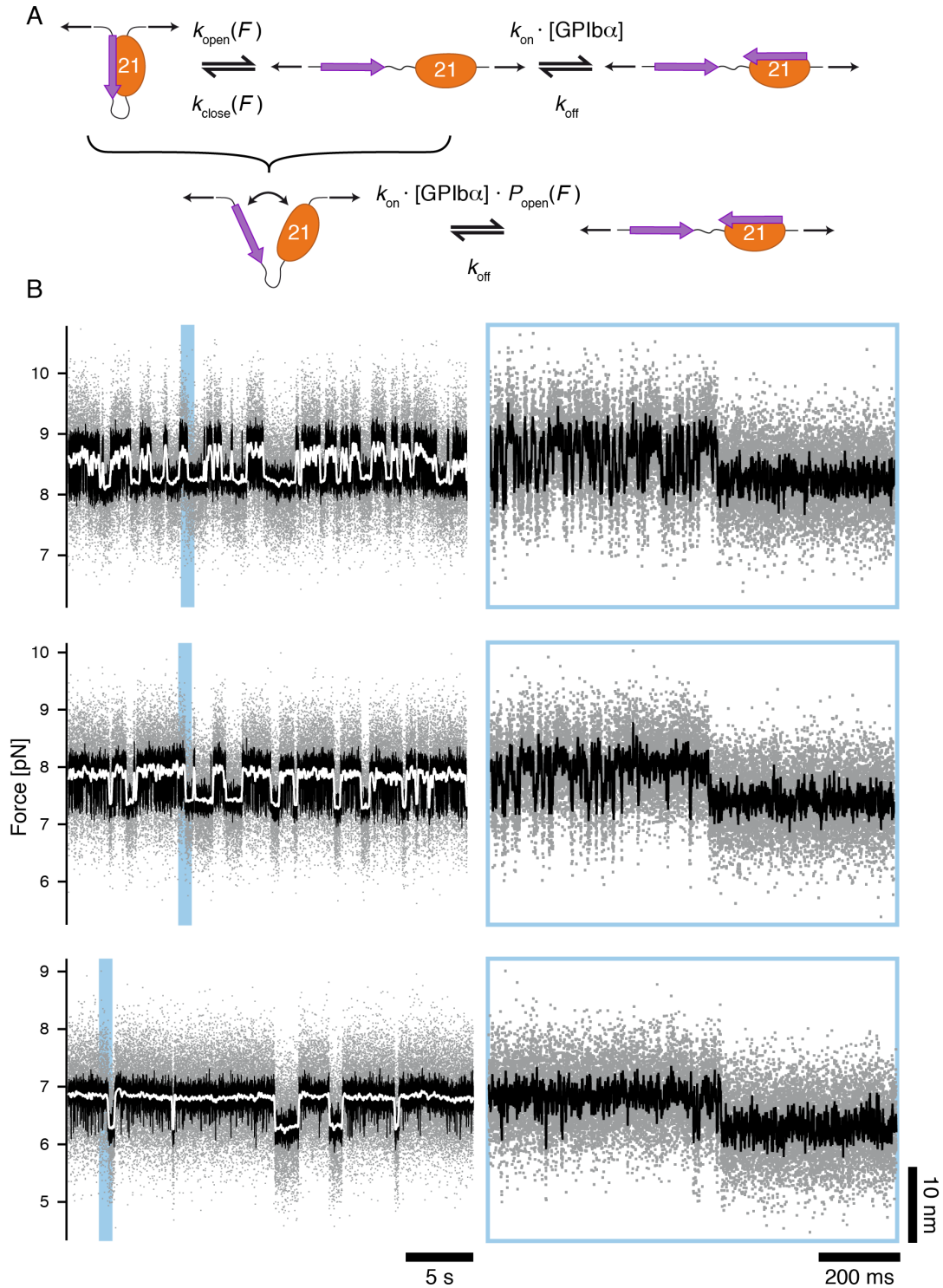
Fig. S3. Single molecule mechanical competition assay. (A) Schematic representation of the rate network. The upper cartoon shows the complete network, while the lower represents the simplified two-state system with the fluctuating (left) and quenched state (right). (B) Three sample traces at different biasing forces. The lowest state has the smallest force and therefore the tethered probe ligand populates the bound (upper) state most of the time. This can be seen in great detail in the zoom region on the right corresponding to the region marked with the light blue filled rectangle in the left trace. Only few quenched states are present. With increasing force (middle and upper traces), the equilibrium of the tethered ligand is shifted more and more to the open state. Therefore, the number of quenched states increases.
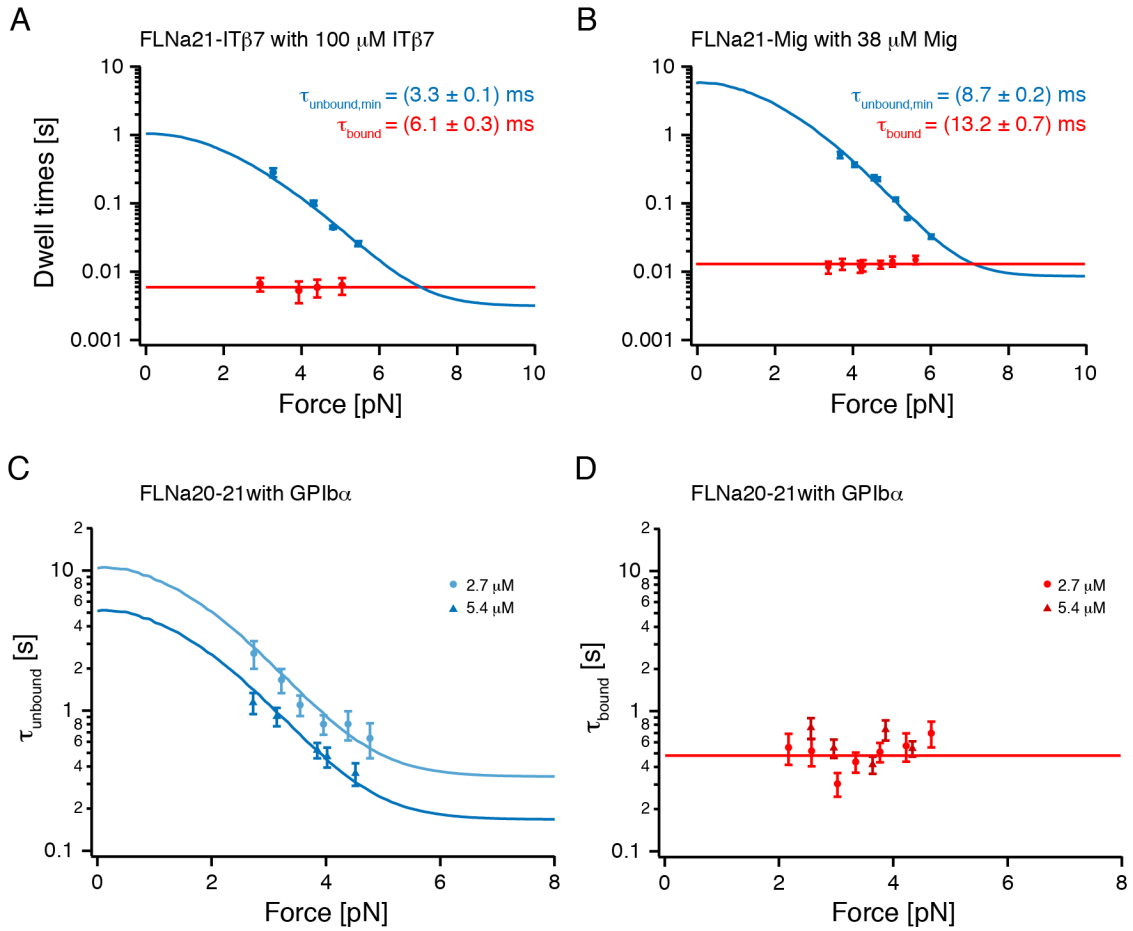
17

Fig. S4. Force dependent dwell times extracted from the single molecule mechanical competition assay. Dwell times of fluctuating (blue) and quenched (red) state of different tethered peptide constructs with corresponding peptides in solution (A, B) and of the double domain construct (FLNa20-21) with GPIbα in solution (C, D). (A) ITβ7 binding is measured in competition with tethered ITβ7. (B) Migfilin binding is measured in competition with tethered migfilin. The solid lines are fits. For the force independent τ_{bound}, a simple line fit is used. For the force dependent $\tau_{unbound}$, the fit is given by the inverse of the equation given in the main text. The resulting optimized fit parameters $\tau_{unbound,min}$ and τ_{bound} are shown. (C) Dwell times of the unbound fluctuating state of FLNa20-21 with GPIbα at two different concentrations. Solid lines are fits (cf. (A, B)). (D) Dwell times of the bound or quenched state of FLNa20-21 for two different concentration of GPIbα. The solid line is a simple line fit.
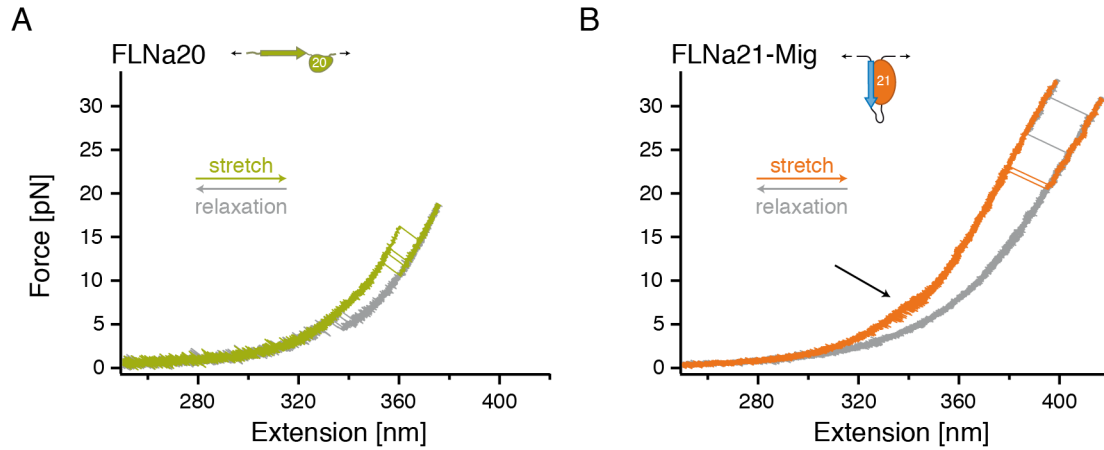
Fig. S5. Single domain force-extension curves of FLNa20 and FLNa21. Colored traces represent extension traces while grey traces show the relaxation. (A) Overlay of four stretch-and-relax cycles (50 nm/s) of one single domain 20 of human filamin A including the A-strand. Unfolding occurs as in the two-domain construct FLNa20-21 (Fig. 4A) at forces around 12 pN suggesting that also in the single domain the A-strand is detached from the rest of the folded domain body. The grey retraction curves display refolding at forces around 5 pN. (B) Overlay of four complete unfolding curves of one single domain 21 of human filamin A with tethered migfilin. At low forces the migfilin binding/unbinding fluctuations (cf. Fig. 2G) are marked by a black arrow. At higher forces (25-30 pN) the unfolding of FLNa21 takes place as in the sample trace of the two-domain construct FLNa20-21. Furthermore, the migfilin peptide allows the demonstration that the peptide-domain interaction is specific for the folded structure of domain 21. After unfolding the grey retraction curve shows no fluctuations compared to the extension trace at the corresponding force range around 6 pN. At zero-load the domain refolds, allowing repeated un- and refolding cycles with the same molecule. The mean unfolding force lies above the sampled maximal force of 35 pN. Therefore unfolding events are rare and also happen during retraction cycles due to the slow moving speed of 10 nm/s.
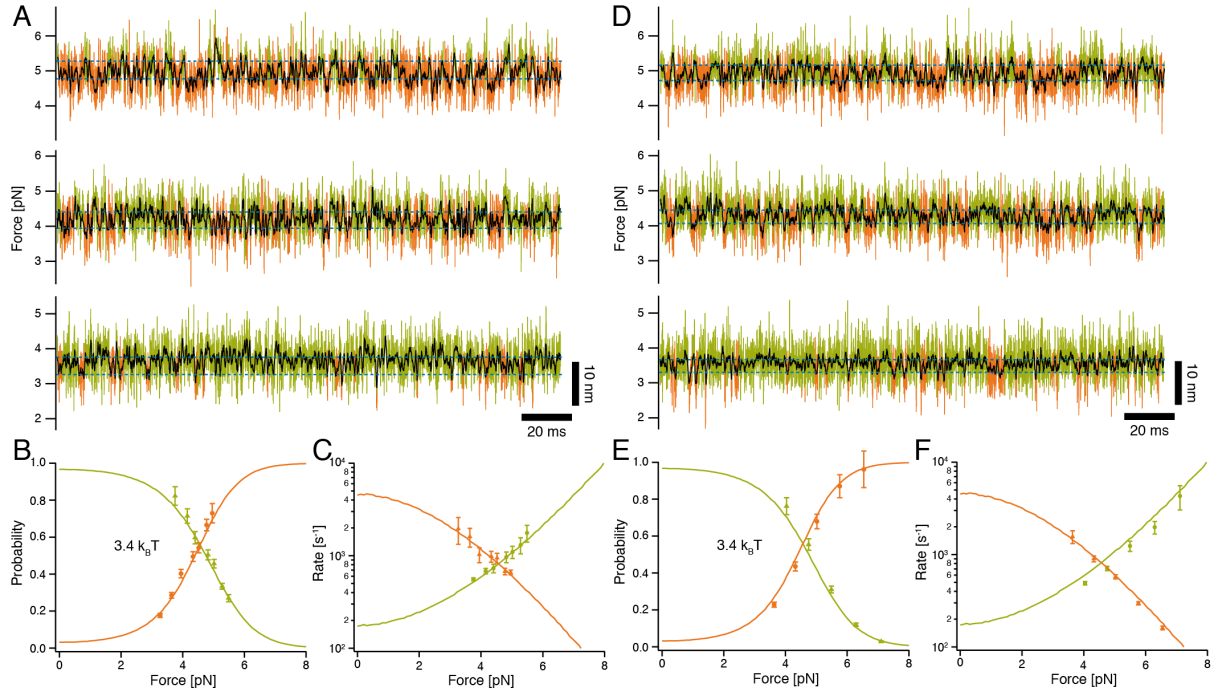
Fig. S6. Kinetic HMM analysis of opening of FLNa20-21. (A) Three sample traces of equilibrium measurements with HMM based assignment of the closed (upper, green) and open (lower, orange) state at three different biasing forces. Blue dashed lines mark state positions. The black line is a moving average of the 20 kHz data (colored lines) with 0.5 ms window size. (B) Force dependent probability of the closed (green triangles) and open (orange circles) state. Solid lines are global fits to Eq. 10 and give the equilibrium free energy difference 3.4 $k_\mathrm{B}T$. (C) Force dependent on- (orange triangles) and off-rates (green circles) of the opening and closing of the domain pair. Zero-force values are extrapolated by fits based on Eq. 11 represented by solid lines. Probabilities of state population do not add up to one due to the different forces for both states (cf. Fig. S2). (D-F) Simulation of the experiment at biasing forces similar to data shown in (A). We performed Brownian dynamics simulations of the experiment with the contour length and kinetic parameters given in Tables S1 and S2, respectively (for details see SI text). The traces were then analyzed with our HMM analysis using the same procedure as for the original data. (D) Three sample traces of simulated equilibrium measurements with HMM based assignment (cf. (A)). (E) Force dependent probability of the simulated closed (green triangles) and open (orange circles) state. Solid lines are global fits to Eq. 10 based on the original data shown in (B). (F) Force dependent on- (orange triangles) and off-rates (green circles) of the simulated opening and closing of the domain pair. Solid lines are the zero-force extrapolations of the original data shown in (C). Probabilities and rate-extrapolation extracted from the original data are in excellent agreement with the values extracted from the simulation.